Hidden higher-order topology in nonsymmorphic group IV and V tetragonal monolayers

Yang Xue [1,*], Wei Xu [2], Bao Zhao,[2,3] and Zhongqin Yang [2,4]

[1]*School of Physics, East China University of Science and Technology, Shanghai 200237, China*
[2]*State Key Laboratory of Surface Physics and Key Laboratory of Computational Physical Sciences (MOE) and
Department of Physics, Fudan University, Shanghai 200433, China*
[3]*Shandong Key Laboratory of Optical Communication Science and Technology, School of Physics Science
and Information Technology, Liaocheng University, Liaocheng 252059, China*
[4]*Shanghai Qi Zhi Institute, Shanghai 200030, China*

In recent years, two-dimensional (2D) second-order topological insulators (SOTIs) have garnered significant interest, with indications of their potential realization in various symmorphic 2D electronic materials. However, up to this point, no nonsymmorphic 2D electronic SOTIs have been identified, probably due to the inability of nonsymmorphic operations to maintain the invariance of nanoflakes. In this paper, we investigate the existence of nonsymmorphic 2D SOTIs, unveiling hidden higher-order topology within 2D nonsymmorphic electronic systems. Our findings are substantiated by symmetry analyses, tight-binding (TB) models, and first-principles calculations. The emergence of topological corner states in these nonsymmorphic 2D SOTIs is attributed to the filling anomaly within a set of symmorphic Wannier orbitals, which exhibit a symmorphic distribution. We identify square-octagon monolayers (so-MLs) of group IV and V elements, including 2D tetragonal P, and 2D hydrogenated tetragonal Si and Ge, as promising material candidates. The corner states in these nonsymmorphic so-MLs are protected by a point symmetry (C_4 rotation). The TB model of so-MLs behaves similarly to the Su-Schrieffer-Heeger model, with higher-order topological insulating phases having greater intersquare hoppings compared to intrasquare hoppings, while the reverse is considered trivial. These discoveries not only enrich our theoretical comprehension of higher-order topology but also introduce potential material candidates for experimental exploration, thus advancing the field of topological crystalline materials.

I. INTRODUCTION

Two-dimensional (2D) second-order topological insulators (SOTIs) represent a novel category within the realm of topological crystalline phases [1–4]. They are characterized by the presence of 1D gapped edge states and 0D in-gap corner states (CSs) [5–12]. In a time-reversal symmetry ($\mathcal{T}$)-preserved 2D SOTI, the existence of CSs is intricately linked to its crystalline symmetries and can be attributed to a filling anomaly [1,13,14]. This filling anomaly arises from the fact that charge neutrality is not compatible with the relevant symmetries respected by the SOTI nanoflake. Up to now, 2D electronic SOTIs have been exclusively proposed within systems exhibiting symmorphic symmetries [6–12]. It is indeed intriguing to inquire whether a nonsymmorphic 2D SOTI exists.

At first glance, the answer to the question posed above appears to be negative, as a nanoflake can only remain invariant under symmorphic symmetries. However, if we take into consideration that in SOTIs, the filling anomaly typically pertains to a set of obstructed charge centers or Wannier centers, the aforementioned question seems to regain its feasibility. A set of charge centers or Wannier centers are considered obstructed or in obstructed atomic limit (OAL), implying a mismatch between these centers and atomic positions [15–20]. For a crystal with nonsymmorphic symmetries, it may possess a set of obstructed Wannier orbitals whose centers' positions remain invariant under the point symmetry parts of the nonsymmorphic symmetries. Consequently, the filling anomaly for these obstructed Wannier orbitals can be associated with a point operation rather than a nonsymmorphic operation, thereby leading to the emergence of CSs protected by this point operation. To illustrate this idea more vividly, we can regard this set of obstructed Wannier centers as an effective lattice that remains invariant under the point operations and the nontrivial higher-order topology is hidden in the filling anomaly for this effective lattice.

In this paper, we extend the theory and material candidates' range of higher-order topology by recognizing that square-octagon monolayers (so-MLs) of group IV and V elements, including 2D tetragonal P (so-P), and 2D hydrogenated tetragonal Si (so-Si) and Ge (so-Ge), a class of well-studied materials [21–26] with nonsymmorphic symmetries, are 2D SOTIs. Based on first-principles calculations and theoretical analysis, the bulk symmetry indicators [14,15,17], Stiefel-Whitney (SW) numbers [27–32], decompositions of atomic-orbital-induced band representations (aBRs) [15,33], CSs, and the tight-binding (TB) model are applied to identify the nontrivial topology. The group IV and V so-MLs are ideal candidates for the experimental realization of 2D hidden SOTIs.
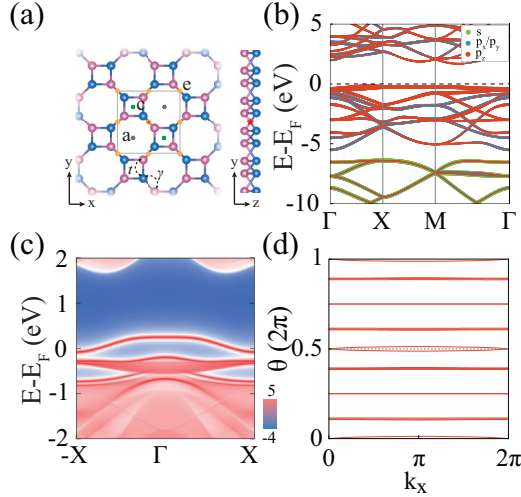
*xuey@ecust.edu.cn

FIG. 1. (a) Optimized geometries of the so-P with maximal Wyckoff positions ($2a$, $2c$, $4e$) in the unit cell, and two types of nearest-neighbor hopping are labeled as t and γ, respectively. The P atoms in different planes are represented by pink and blue spheres. The red star denotes the inversion center. (b) Orbital-resolved bands of so-P. Red dots: p_z orbitals; blue dots: $p_{x,y}$ orbitals; and green dots: s orbitals. (c) The projected spectra for the (100) edge of a semi-infinite sheet of the so-P. (d) The 1D k_y-direct Wilson bands as a function of k_x calculated in the density functional theory (DFT) code.

II. RESULTS AND DISCUSSION

The group IV and V so-MLs are a new class of 2D tetragonal allotrope, which are reported to be stable semiconductors [21–26]. These so-MLs own a similar buckled square geometric structure [Fig. 1(a)] with a space group of $P4/nbm$ (No. 125) and a point group of D_{4h}. Due to similar crystal structures and electronic properties, we will use so-P as a representative, while the relevant results for other materials can be found in the Supplemental Material (SM) [34]. The unit cell of the so-P has eight P atoms, where there are four P atoms in the upper plane (blue spheres) while the other four atoms are in the lower plane (pink spheres), as displayed in Fig. 1(a). The optimized lattice constant of the so-P is 6.54 Å, consistent with the previous results [21–24]. In so-P, each P atom forms π bonding and σ bonding with its nearest neighbors [21], resulting in a stable noncoplanar structure. This is confirmed by the phonon spectrum calculations and molecular dynamics simulations [21,22]. There are three kinds of maximal Wyckoff positions $2a$, $2c$, and $4e$ in this unit cell, labeled with gray hexagons, green squares, and yellow circles in Fig. 1(a), respectively.

Figure 1(b) displays the calculated orbital-resolved energy bands, where the s bands and p bands under the Fermi level (E_F) exhibit a clear separation between them. Since the energy gap at the E_F is very large and the spin-orbit coupling in this so-P is small [34], it can be effectively neglected, allowing the material to be treated as spinless in later discussions. As shown in Fig. 1(c), the relatively flat and gapped edge state of the semi-infinite plane of the so-P along the (100) direction demonstrates that the so-P is not a traditional topological insulator. Because the spinless so-P possesses a space-time

TABLE I. BR decompositions for the occupied bands of the so-P. The first two columns indicate whether the s and p bands can be decomposed into aBRs (eBRs). The third column provides the specific decomposition results, and the last two columns present the corresponding SW numbers of each decomposition, obtained by parity criterion. The third row provides the SW numbers for all the eBRs appearing in the decompositions of p bands, where a_i (c_i) refers to any one of A_1, B_1, and E. Details of the decompositions and irreps of the occupied bands can be found in the SM [34].

	aBRs	eBRs	Decompositions		w_1	w_2
p bands	×	✓	D1	$A_g@4e\oplus$ $(A_1 \oplus B_1 \oplus E)@2c$	0	1
			D2	$A_g@4e\oplus$ $(A_1 \oplus B_1 \oplus E)@2a$	0	1
				$A_g@4e$	0	1
				$a_i@2a$ ($c_i@2c$)	0	0
s bands	✓			$A'@8m$	0	0

inversion symmetry ($\mathcal{IT}$, where $\mathcal{I}$ represent inversion symmetry), its second-order band topology can be described by the second Stiefel-Whitney (SW) number (w_2) [27–32]. The second SW number w_2 is a well-defined 2D topological invariant of an insulator only when the first SW number $w_1 = 0$. Here, the w_1 is defined as

$$w_1|_C = \frac{1}{\pi} \oint_C d\mathbf{k} \cdot \mathrm{Tr}\,\mathcal{A}(\mathbf{k}), \qquad (1)$$

where $\mathcal{A}_{mn} = \langle u_m(\mathbf{k})|i\nabla_{\mathbf{k}}|u_n(\mathbf{k})\rangle$ [30]. The second SW class (w_2) can be computed by three methods: the parity criterion, the nested Wilson-loop method, or simply by m module 2, where m is the number of crossings of Wilson bands at $\theta = \pi$ [9,12]. As illustrated in Fig. 1(d), the Wilson bands for all occupied energy bands exhibit symmetric distribution with respect to $\theta = \pi$, implying that $w_1 = 0$, which is a necessary condition for a well-defined w_2. There is one crossing of Wilson bands at $\theta = \pi$ in Fig. 1(d), indicating the second SW class $w_2 = 1$. Therefore, the so-P is a SOTI with a nontrivial w_2. It is noteworthy that all rotational and mirror symmetries of the buckled so-P are nonsymmorphic (with our unit cell choice), meaning that there are no symmetry operations that would keep the nanoflakes of so-P invariant and, consequently, protect CSs. To comprehend the higher-order topological mechanisms of this system and identify the corresponding symmetries that can protect CSs, we employed topological quantum chemistry [15,16] to analyze the electronic states of the system in the following. This analysis revealed the existence of hidden higher-order topology within this system.

As we mentioned above, the OAL serves as a key signature of 2D SOTIs, which can be diagnosed through their band representations (BRs). The absence of the decomposition of BRs into aBRs is referred to as OAL, indicating that the BRs can be decomposed into elementary BRs (eBRs), but not aBRs [15,17]. We first calculated the irreducible representations (irreps) for the occupied bands at several high-symmetry k points and their BR decompositions. As shown in Table I, the s bands can be decomposed as an aBR, while the p bands cannot be decomposed as a sum of aBRs, but can

be decomposed as a sum of eBRs induced from maximal Wyckoff positions $4e$ and $2a$ ($2c$), respectively. Hence the nontrivial topology of so-P is derived from the p bands. The two decompositions of eBRs for the p bands, D1 and D2, consist of $A_g@4e$ along with either $(A_1 \oplus B_1 \oplus E)@2a$ or $(A_1 \oplus B_1 \oplus E)@2c$, respectively. Because $(A_1 \oplus B_1 \oplus E)@2a$ and $(A_1 \oplus B_1 \oplus E)@2c$ are equivalent, as demonstrated below, D1 and D2 are indeed identical. The site symmetry groups of Wyckoff positions $2a$ and $2c$ are D_4 and D_{2d}, respectively. The straight lines connecting $2a$ with $2c$ own a site symmetry group of C_2. Due to the relations

$$C_2 \subset (D_4 \cap D_{2d}),$$
$$2(A \oplus B)\uparrow D_4 = A_1 \oplus B_1 \oplus E,$$
$$2(A \oplus B)\uparrow D_{2d} = A_1 \oplus B_1 \oplus E, \tag{2}$$

where the A and B are the two irreps of the C_2 (see details in SM [34]), respectively, $(A_1 \oplus B_1 \oplus E)@2a$ and $(A_1 \oplus B_1 \oplus E)@2c$ are equivalent [15,16].

For a set of bands with $\mathcal{I}$ and $\mathcal{T}$, the corresponding polarization can be derived from the inversion eigenvalues of these bands [13,35,36]. In our system, the polarization can be expressed specifically as

$$p_x \overset{\mathcal{I}}{=} \begin{cases} 0, & \text{if } \mathcal{I}(\Gamma)\mathcal{I}^*(X) = +1 \text{ and } \mathcal{I}(Y)\mathcal{I}^*(M) = +1, \\ 1/2, & \text{if } \mathcal{I}(\Gamma)\mathcal{I}^*(X) = -1 \text{ and } \mathcal{I}(Y)\mathcal{I}^*(M) = -1, \end{cases} \tag{3}$$

and

$$p_y \overset{\mathcal{I}}{=} \begin{cases} 0, & \text{if } \mathcal{I}(\Gamma)\mathcal{I}^*(Y) = +1 \text{ and } \mathcal{I}(X)\mathcal{I}^*(M) = +1, \\ 1/2, & \text{if } \mathcal{I}(\Gamma)\mathcal{I}^*(Y) = -1 \text{ and } \mathcal{I}(X)\mathcal{I}^*(M) = -1. \end{cases} \tag{4}$$

As shown in Table S2, all the decomposed eBRs of p bands have a polarization (p_x, p_y) of zero, indicating that their w_1 is zero. Therefore, for each decomposed eBR, its w_2 is individually well defined, enabling us to discern the relationship between the nontrivial topological properties of the system and these eBRs. For this purpose, we can further determine the w_2 of these eBRs using the parity criterion as

$$(-1)^{w_2} = \prod_{\Pi \in \text{TRIM}} (-1)^{\lfloor N_{\text{occ}}^-(\Pi)/2 \rfloor}, \tag{5}$$

where the $\lfloor \cdot \rfloor$ is the floor function. From the results shown in Table I, we can see that the $A_g@4e$ hold a nontrivial $w_2 = 1$, while the other eBRs are all topologically trivial ($w_2 = 0$). This suggests that the nontrivial topology of the systems is actually derived from the $A_g@4e$ eBR. It is also noticed that the sites of the $4e$ Wyckoff position are distributed in the same plane and are invariant under symmorphic rotation symmetry C_{4z}. Thus the nonsymmorphic so-P owns a hidden nontrivial topology, whose CSs arise from the filling anomaly of the Wannier orbitals on $4e$ sites and are protected by the C_{4z} symmetry.

To verify the nontrivial topological properties of the so-P, we further calculated its symmetry indicators and topological CSs. Due to the nontrivial topology of the so-P being related to the C_{4z} symmetry, the symmetry indicators and related corner
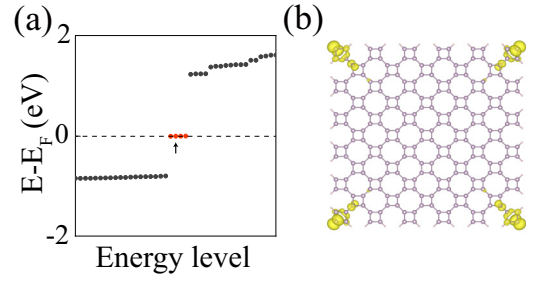

FIG. 2. (a) Calculated energy spectra for the so-P flake shown in (b) with DFT code. Red and black dots represent corner and bulk states. The black arrow denotes the Fermi levels by the electron counting, E_F. (b) The so-P flake, in which the charge distributions of the corner states are also shown. The isosurface value is set as $0.003\, e\, \text{Å}^{-3}$.

charges for the so-P can be expressed as

$$\chi^{(4)} = \left([X_1^{(2)}], [M_1^{(4)}], [M_2^{(4)}]\right),$$
$$Q_{\text{corner}}^{(4)} = \frac{e}{4}\left([X_1^{(2)}] + 2[M_1^{(4)}] + 3[M_2^{(4)}]\right) \bmod e. \tag{6}$$

Here, the superscript 4 in $\chi^{(4)}$ and $Q_{\text{corner}}^{(4)}$ denotes the C_4 symmetry, and the invariant $[\Pi_p^{(n)}]$, $\Pi = X$, or M indicates the difference in the number of eigenvalues ($e^{2\pi i(p-1)/n}$) of the C_n operation at Π and Γ in the occupied band manifold [14]. The symmetry indicators for all the occupied bands of the so-P are determined to be $\chi^{(4)} = (-2, 0)$, confirming that so-P is a SOTI. Symmetry indicators calculated using only the $A_g@4e$ eBR are the same as those calculated using all occupied bands of the so-P, indicating that its nontrivial topological properties are indeed determined by the $A_g@4e$ eBR, consistent with the above analysis.

The obtained $\chi^{(4)} = (-2, 0)$ indicates that for a so-P flake, when the $4e$ lattice points within it exhibit C_4 symmetry, and the edges of the flake terminate at the $4e$ sites, a corner charge of $Q_{\text{corner}}^{(4)} = e/2$ is observed. By calculating this flake, approximately fourfold degenerate states [red circles in Fig. 2(a)] emerge around the E_F. Their charge distributions are all localized around the corners of the flake, as shown in Fig. 2(b). Since only half of the CSs are occupied [Fig. 2(a)], an average spinless corner charge of $e/2$ is obtained, in line with the symmetry indicators.

Considering that, as shown in Fig. 1(b), the low-energy bands near the E_F are primarily contributed by the p_z orbitals, in order to gain a deeper understanding of the low-energy physics of the so-P, we have constructed a symmetry-constrained TB Hamiltonian with a p_z orbital per P atom site as

$$H = t \sum_{\substack{\langle i,j \rangle \\ t \in \text{intrasquare}}} C_i^\dagger C_j + \gamma \sum_{\substack{\langle i,j \rangle \\ \gamma \in \text{intersquare}}} C_i^\dagger C_j + \text{H.c.} \tag{7}$$

Details regarding the derivations of the parameters for the TB model can be found in SM [34]. As displayed in Fig. 1(a), there are two types of nearest hopping parameters in this model: intrasquare hopping (t) and intersquare hopping (γ). Figures 3(a) and 3(d) show the bands of the two insulating phase for our TB model with γ/t equal to 2.5 and 0.5,
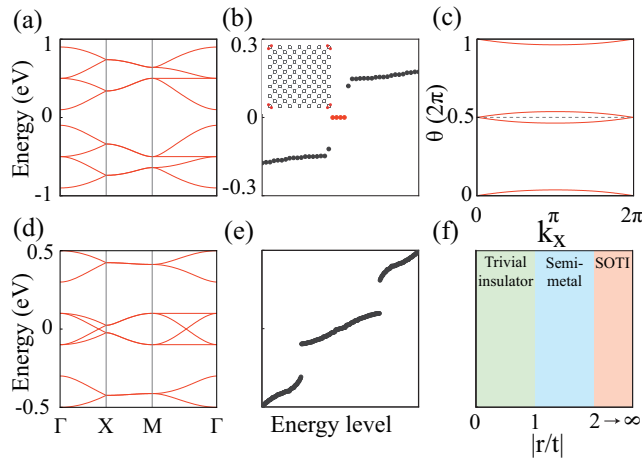
FIG. 3. (a) and (d) depict the electronic band structures for our TB model with the parameters $\gamma/t = 2.5$ and $\gamma/t = 0.5$, respectively. (b) and (e) display the energy spectra of the nanoflakes of the TB model with identical parameters as those in (a) and (d), respectively. Red and black dots represent corner and bulk states, respectively. The inset in (b) shows the flake shape and the charge distributions of the corner states. (c) is the 1D k_y-direct Wilson bands as a function of k_x calculated for the lowest four bands of (a). (f) presents the phase diagram of the TB model.

respectively. Flake calculations for the TB model with different parameters demonstrate that, for $\gamma/t = 0.5$ [Fig. 3(e)], no CSs emerge in either energy gap. However, for $\gamma/t = 2.5$ [Fig. 3(b)], fourfold degenerate states (depicted as red circles) emerge within the energy gap, confirming that the half-filled TB model with these parameters is in the SOTI phase. The nontrivial topology of this case is further confirmed by the Wannier band calculations [Fig. 3(c)], yielding $w_2 = 1$. It is also worth noting that within the parameter region $\gamma/t > 2$, the BR decompositions for the half-filled TB model are identical to $A_g@4e$, demonstrating that this model captures the nontrivial topological properties of the system. We have further computed the band structures and corresponding

topological properties of the TB model as it evolves with parameters, and the phase diagram is presented in Fig. 3(f). The phase diagram shows that our TB model behaves similarly to the Su-Schrieffer-Heeger (SSH) model, with higher-order topological insulating phases having greater intersquare hoppings compared to intrasquare hoppings, while the reverse is considered trivial. The differentiation between intersquare hoppings and intrasquare hoppings in the so-P monolayer originates from its buckled square geometric structure. This structure also gives rise to the emergence of nonsymmorphic geometries within the so-P monolayer, highlighting the intrinsic connection between nonsymmorphic symmetries and the nontrivial topology present in the so-P monolayer.

Our findings therefore reveal the hidden higher-order topology in the 2D nonsymmorphic systems, supported by a symmetry analysis, tight-binding models, and first-principles calculations. The emergence of topological CSs in these nonsymmorphic 2D SOTIs is attributed to the filling anomaly of a set of symmorphic Wannier orbitals, and these CSs are protected by the corresponding point symmetries. We identify group IV and V nonsymmorphic so-MLs as suitable material candidates, whose corner states are protected by a point symmetry (C_4). The TB model unveils a topological behavior in the so-MLs akin to that of the SSH model, where higher-order topological insulating phases exhibit greater intersquare hoppings than intrasquare hoppings. These results not only extend the theoretical framework and range of material candidates for 2D SOTIs but also provide several potential candidates for the experimental realization of 2D SOTIs in nonsymmorphic electronic systems.

[1] W. A. Benalcazar, B. A. Bernevig, and T. L. Hughes, Quantized electric multipole insulators, Science **357**, 61 (2017).

[2] F. Schindler, A. M. Cook, M. G. Vergniory, Z. Wang, S. S. P. Parkin, B. A. Bernevig, and T. Neupert, Higher-order topological insulators, Sci. Adv. **4**, eaat0346 (2018).

[3] B. Xie, H.-X. Wang, X. Zhang, P. Zhan, J.-H. Jiang, M. Lu, and Y. Chen, Higher-order band topology, Nat. Rev. Phys. **3**, 520 (2021).

[4] B. J. Wieder, B. Bradlyn, J. Cano, Z. Wang, M. G. Vergniory, L. Elcoro, A. A. Soluyanov, C. Felser, T. Neupert, N. Regnault, and B. A. Bernevig, Topological materials discovery from crystal symmetry, Nat. Rev. Mater. **7**, 196 (2022).

[5] M. Ezawa, Higher-order topological insulators and semimetals on the breathing kagome and pyrochlore lattices, Phys. Rev. Lett. **120**, 026801 (2018).

[6] X.-L. Sheng, C. Chen, H. Liu, Z. Chen, Z.-M. Yu, Y. X. Zhao, and S. A. Yang, Two-dimensional second-order topological insulator in graphdiyne, Phys. Rev. Lett. **123**, 256402 (2019).

[7] B. Liu, G. Zhao, Z. Liu, and Z. F. Wang, Two-dimensional quadrupole topological insulator in γ-graphyne, Nano Lett. **19**, 6492 (2019).

[8] J. Zeng, H. Liu, H. Jiang, Q.-F. Sun, and X. C. Xie, Multiorbital model reveals a second-order topological insulator in 1H transition metal dichalcogenides, Phys. Rev. B **104**, L161108 (2021).

[9] S. Qian, C.-C. Liu, and Y. Yao, Second-order topological insulator state in hexagonal lattices and its abundant material candidates, Phys. Rev. B **104**, 245427 (2021).

[10] S. K. Radha and W. R. L. Lambrecht, Buckled honeycomb antimony: Higher order topological insulator and its relation to the Kekulé lattice, Phys. Rev. B **102**, 115104 (2020).

[11] Y. Xue, H. Huan, B. Zhao, Y. Luo, Z. Zhang, and Z. Yang, Higher-order topological insulators in two-dimensional Dirac materials, Phys. Rev. Res. **3**, L042044 (2021).

[12] Z. Guo, J. Deng, Y. Xie, and Z. Wang, Quadrupole topological insulators in Ta$_2$M$_3$Te$_5$ ($M =$ Ni, Pd) monolayers, npj Quantum Mater. **7**, 87 (2022).

[13] W. A. Benalcazar, B. A. Bernevig, and T. L. Hughes, Electric multipole moments, topological multipole moment pumping, and chiral hinge states in crystalline insulators, Phys. Rev. B **96**, 245115 (2017).

[14] W. A. Benalcazar, T. Li, and T. L. Hughes, Quantization of fractional corner charge in C_n-symmetric higher-order topological crystalline insulators, Phys. Rev. B **99**, 245151 (2019).

[15] B. Bradlyn, L. Elcoro, J. Cano, M. G. Vergniory, Z. Wang, C. Felser, M. I. Aroyo, and B. A. Bernevig, Topological quantum chemistry, Nature (London) **547**, 298 (2017).

[16] J. Cano, B. Bradlyn, Z. Wang, L. Elcoro, M. G. Vergniory, C. Felser, M. I. Aroyo, and B. A. Bernevig, Building blocks of topological quantum chemistry: Elementary band representations, Phys. Rev. B **97**, 035139 (2018).

[17] H. C. Po, A. Vishwanath, and H. Watanabe, Symmetry-based indicators of band topology in the 230 space groups, Nat. Commun. **8**, 50 (2017).

[18] F. Tang, H. C. Po, A. Vishwanath, and X. Wan, Comprehensive search for topological materials using symmetry indicators, Nature (London) **566**, 486 (2019).

[19] T. Zhang, Y. Jiang, Z. Song, H. Huang, Y. He, Z. Fang, H. Weng, and C. Fang, Catalogue of topological electronic materials, Nature (London) **566**, 475 (2019).

[20] Z. Song, Z. Fang, and C. Fang, $(d-2)$-dimensional edge states of rotation symmetry protected topological states, Phys. Rev. Lett. **119**, 246402 (2017).

[21] F. Ersan, E. Aktürk, and S. Ciraci, Stable single-layer structure of group-V elements, Phys. Rev. B **94**, 245417 (2016).

[22] P. Li and W. Luo, A new structure of two-dimensional allotropes of group V elements, Sci. Rep. **6**, 25423 (2016).

[23] S. Ghosal and D. Jana, Beyond T-graphene: Two-dimensional tetragonal allotropes and their potential applications, Appl. Phys. Rev. **9**, 021314 (2022).

[24] Y. Zhang, J. Lee, W.-L. Wang, and D.-X. Yao, Two-dimensional octagon-structure monolayer of nitrogen group elements and the related nano-structures, Comput. Mater. Sci. **110**, 109 (2015).

[25] C. Xu, J. Zhang, M. Guo, and L. Wang, Modulation of the electronic property of hydrogenated 2D tetragonal Ge by applying external strain, RSC Adv. **9**, 23142 (2019).

[26] H. Tu, J. Zhang, Z. Guo, and C. Xu, Biaxial strain modulated the electronic structure of hydrogenated 2D tetragonal silicene, RSC Adv. **9**, 42245 (2019).

[27] Y. X. Zhao and Y. Lu, PT-symmetric real Dirac fermions and semimetals, Phys. Rev. Lett. **118**, 056401 (2017).

[28] Y. X. Zhao, A. P. Schnyder, and Z. D. Wang, Unified theory of PT and CP invariant topological metals and nodal superconductors, Phys. Rev. Lett. **116**, 156402 (2016).

[29] C. Fang, Y. Chen, H.-Y. Kee, and L. Fu, Topological nodal line semimetals with and without spin-orbital coupling, Phys. Rev. B **92**, 081201(R) (2015).

[30] J. Ahn, S. Park, D. Kim, Y. Kim, and B.-J. Yang, Stiefel–Whitney classes and topological phases in band theory, Chin. Phys. B **28**, 117101 (2019).

[31] J. Ahn, S. Park, and B.-J. Yang, Failure of Nielsen-Ninomiya theorem and fragile topology in two-dimensional systems with space-time inversion symmetry: application to twisted bilayer graphene at magic angle, Phys. Rev. X **9**, 021013 (2019).

[32] J. Ahn, D. Kim, Y. Kim, and B.-J. Yang, Band topology and linking structure of nodal line semimetals with Z_2 monopole charges, Phys. Rev. Lett. **121**, 106403 (2018).

[33] J. Gao, Y. Qian, H. Jia, Z. Guo, Z. Fang, M. Liu, H. Weng, and Z. Wang, Unconventional materials: The mismatch between electronic charge centers and atomic positions, Sci. Bull. **67**, 598 (2022).

[34] See Supplemental Material at http://link.aps.org/supplemental/10.1103/PhysRevB.109.075115 for the results of the group IV tetragonal monolayers, computational methods, tight-binding models, and symmetry analysis, which includes Refs. [37–41].

[35] T. L. Hughes, E. Prodan, and B. A. Bernevig, Inversion-symmetric topological insulators, Phys. Rev. B **83**, 245132 (2011).

[36] A. M. Turner, Y. Zhang, R. S. K. Mong, and A. Vishwanath, Quantized response and topology of magnetic insulators with inversion symmetry, Phys. Rev. B **85**, 165120 (2012).

[37] A. A. Mostofi, J. R. Yates, Y.-S. Lee, I. Souza, D. Vanderbilt, and N. Marzari, Wannier90: A tool for obtaining maximally-localised Wannier functions, Comput. Phys. Commun. **178**, 685 (2008).

[38] Q. Wu, S. Zhang, H.-F. Song, M. Troyer, and A. A. Soluyanov, WannierTools: An open-source software package for novel topological materials, Comput. Phys. Commun. **224**, 405 (2018).

[39] J. Gao, Q. Wu, C. Persson, and Z. Wang, Irvsp: To obtain irreducible representations of electronic states in the VASP, Comput. Phys. Commun. **261**, 107760 (2021).

[40] G. Kresse and J. Furthmüller, Efficient iterative schemes for *ab initio* total-energy calculations using a plane-wave basis set, Phys. Rev. B **54**, 11169 (1996).

[41] J. P. Perdew, K. Burke, and M. Ernzerhof, Generalized gradient approximation made simple, Phys. Rev. Lett. **77**, 3865 (1996).